An adaptive floating node based formulation for the analysis of multiple delaminations under quasi-static loading

Trabal, Guillem Gall; Bak, Brian Lau Verndal; Chen, Boyang; Lindgaard, Esben

Citation (APA)
Trabal, G. G., Bak, B. L. V., Chen, B., & Lindgaard, E. (2022). An adaptive floating node based formulation for the analysis of multiple delaminations under quasi-static loading. *Composites Part A: Applied Science and Manufacturing*, *156*, Article 106846. https://doi.org/10.1016/j.compositesa.2022.106846

Important note
To cite this publication, please use the final published version (if applicable).
Please check the document version above.

An adaptive floating node based formulation for the analysis of multiple delaminations under quasi-static loading

Guillem Gall Trabal [a], Brian Lau Verndal Bak [a], Boyang Chen [b], Esben Lindgaard [a],*

[a] *Department of Materials and Production, Aalborg University, Fibigerstraede 16, DK-9220 Aalborg East, Denmark*
[b] *Faculty of Aerospace Engineering, Delft University of Technology, Kluyverweg 1, 2629 HS Delft, Netherlands*

ARTICLE INFO

ABSTRACT

A novel and efficient numerical formulation for the modelling of multiple delaminations growth in laminated composite materials subjected to quasi-static loading is presented. The proposed formulation alleviates the high computational cost associated with models featuring cohesive elements by using a novel Adaptive Refinement Scheme and an Adaptive Floating Node Method Element to refine the model effectively during the analysis without modifying the global finite element connectivity. The formulation has been implemented in a MATLAB finite element code and validated with single and multiple delamination numerical models with varying mode mixities. The new formulation provides accurate results comparable to standard fully refined finite element models while drastically lowering the computational time of the analysis.

1. Introduction

Delamination is one of the most common damage modes leading to the final failure of laminated composite structures. Current models accounting for delamination growth can be separated into those making use of Linear Elastic Fracture Mechanics (LEFM) concepts and those using cohesive formulations [1]. In the LEFM approach, the damage is propagated when the energy release rate G or the stress intensity factor K is equal or larger than its critical values G_c or K_c [2,3]. The values of G_c and K_c are material parameters extracted from experiments while G and K may be calculated in numerical models with tools such as the virtual crack closure technique [4] or the J-integral [5,6]. The main disadvantages of the LEFM approach are its limitation to small fracture process zones and the necessity of two separate criteria for onset and propagation of delamination cracks. On the other hand, Cohesive Zone Models (CZM) [7–9] combine the fracture mechanics concepts with damage mechanics by defining a Damage Process Zone (DPZ), where interface stiffness degradation occurs. The introduction of a CZM avoids the oscillating stress singularity while unifying onset and propagation in a single formulation. CZMs also enable a straightforward and accurate evaluation of the mode decomposed energy release rate for large DPZs using the J-integral [5,10,11]. Delamination is a complex problem that depends on the structural geometry, material configuration and loading conditions. Therefore, Finite Element Analysis (FEA) is typically used through the application of the aforementioned mechanical models. Numerical solutions based on purely fracture mechanics concepts can be implemented directly in an FEA framework.

The CZM based models are most commonly implemented in the finite element method as zero thickness cohesive elements (CE) [12–24]. For laminated composite materials, the cohesive elements normally use standard isoparametric interpolation functions to represent the opening displacement field between the crack surfaces of the two layers.

Even though cohesive elements are often preferred to model delamination onset and growth, numerous challenges which limit their usage remain. One of the most limiting factors is that large variations of the traction field in the DPZ where damage is occurring, and its vicinity, enforces the need for a fine element discretization. This particular zone with a large variation of the traction field is referred hereafter as the high gradient zone. The studies presented in [25,26] have shown that fine meshes are needed to represent the large variations of the traction profile in the high gradient zone. This problem is greatly reduced in mode II due to a geometrically larger DPZ which implies a larger high gradient zone. Studies in literature conclude that, depending on the problem, between 3 to 10 cohesive elements are needed in the DPZ to offer accurate results with acceptable convergence rates [25,27–30]. The remaining part of the traction profile, where tractions vary more moderately is usually discretized with an equally fine mesh, which is inefficient. The high gradient zone and the area with a more moderate variation of the traction profile is often referred as the active part of the cohesive zone, being the cohesive zone any area of the model meshed with cohesive elements. Given the small size of DPZ for commonly used composite material systems, the number of cohesive elements,

and thus also adjacent solid finite elements, increases dramatically with larger models making predictive delamination simulations of large scale composite structures computationally costly or even infeasible.

The fine mesh requirement problem can be alleviated by tweaking the interface properties, modifying the numerical integration of the element or improving the kinematics of the element. In [25] a method to reduce the strength of the interface to artificially enlarge the DPZ allowing the use of coarser CEs is proposed. However, decreasing too much the interface strength can produce inaccurate results [31,32]. Another possibility is using an element with an adaptive numerical integration scheme, which is linked to the damage state of the element, as proposed in [32–35]. This enables the use of slightly larger cohesive elements, but the poor kinematic representation of the crack opening and its implications on the tractions representation limits the benefits. Element enrichments that improve the kinematics of the crack opening profile for low order elements have been proposed in [36–38]. Although accurate results have been obtained, the enrichments are associated with a considerable computational cost [39]. Promising results have been presented by combining accurate kinematic representation of the crack opening using high order structural elements with an adaptive integration scheme in [26].

Another approach to reduce the number of elements is to only have a fine element discretization near the high traction gradient zone by means of remeshing techniques. Remeshing techniques for refinement have been applied successfully in [40–42], but with a limited increase of the overall computational efficiency. The main drawback of remeshing techniques is that a modification of the global connectivity matrix of the finite element model is required when the remeshing operations are performed, which can have an added computational cost depending on the pursued implementation.

For all the aforementioned cohesive element based approaches all the potential crack paths are predefined and discretized with cohesive elements forming a cohesive zone where damage can propagate. However, for large scale structural analysis many of these potential crack paths defined a priori will be inactive for a large part of the analysis or even remain inactive for the entire analysis. For complex delamination cases, such as those featuring multiple delaminations, it is difficult if not impossible to estimate the final crack extension and location prior to the analysis. To address this issue, methods that dynamically add cohesive elements to specific interfaces during the execution of the analysis have been suggested. Such methods include remeshing based techniques for adding cohesive elements during analysis [43,44] or element splitting formulations using local enrichments such as the Phantom Node Method [45,46] and the X-FEM method [38,47].

An alternative formulation is the Floating Node Method (FNM) [48], which can be used to dynamically add CEs as done in [49] for a structural shell element or in [50,51] for solid elements. Compared to X-FEM and the Phantom Node Methods the FNM is simpler as it relies on standard finite element formulations and represents better the geometry of the crack for the same number of degrees of freedom [48]. Operations are done on the element level and since global connectivities are preserved throughout the analysis, the FNM can be more efficient than remeshing techniques, depending on the specific implementation. A refinement method for the FNM has been presented for delamination in double cantilever beam (DCB) specimens with possible crack migration [52]. In that work coarse CEs are placed a priori at desired interfaces and a refinement region, also referred to as a refinement mask, is introduced which moves across the structure as damage evolves and the delamination crack tip propagates. The size of the fixed refinement mask is however based on simple a priori theoretical DPZ length calculations rendering the approach non-generalizable for arbitrarily loaded composite structures.

In this paper a novel efficient adaptive mesh and solution strategy for the analysis of progressive delamination growth in laminated materials is proposed. This work draws inspiration from previous work on the A-FNM element [50,52], but proposes novel improvements that

allow the handling of multiple simultaneous delaminations, the use of a transition zone (with CEs but no longitudinal refinement) and the automatic adaptation of the refined area length to changes in the DPZ's length during the analysis. The adaptive finite element mesh is effectively achieved by the Floating Node Method (FNM) [48] exploiting the key properties of maintaining the finite element bookkeeping for efficient manipulation during the execution of the analysis while relying on underlying standard finite element formulations. The core of the formulation includes a new Adaptive FNM based element (A-FNM) that can be partitioned with cohesive interface elements and refined when needed, and a novel Adaptive Refinement Scheme (ARS). Moreover, unlike the work proposed in [50,52] a single A-FNM element can model the entire thickness of a laminate. The adaptive refinement scheme is capable of efficiently tracking changes in the DPZ length during the analysis without user intervention, enabling the possibility of simulating complex multiple delamination scenarios with a limited zone of cohesive elements. In addition, the presented formulation allows efficient analysis without any prior knowledge of the final crack extension and location.

The article is organized as follows. The A-FNM element is presented in Section 2 together with the general details of the FEA framework developed for its implementation. Next, Section 3 introduces the new adaptive refinement scheme. Finally, Section 4 provides a series of benchmarks to show the accuracy of the results, the improvement in computational time, and the capabilities of the formulation. Conclusions are outlined in Section 5.

2. The Adaptive-FNM element

The A-FNM element can automatically refine, coarsen and split itself into 2D solid and interface elements to improve accuracy, convergence and numerical efficiency during execution, while obeying compatibility to non-refined zones by auto-generated Multi-Point Constraints (MPC). The underlying element technologies for the framework are a 2D layered 4-noded, geometrically linear, plane strain, Enhanced Assumed Strains stabilized solid element (EAS-4) based on [53,54], and a 4-noded zero-thickness interface element [22,55], which includes a progressive interlaminar damage formulation based on a bilinear cohesive law and is formulated by an updated Lagrangian approach accounting for geometrically non-linear effects. Remark that the main methodologies used for the A-FNM element are inherited from the original work presented in [48] with additions to obtain the desired formulation for the A-FNM element.

2.1. Floating node method implementation for local mesh refinement

As proposed in [48], the A-FNM element is initialized with a set of standard nodes that are active throughout the analysis and a set of floating nodes (FNs) which can be activated and deactivated as required. Initially, the FNs do not have an assigned position and can be initialized, for instance, at the global origin of coordinates. All the FNs are connected to an element meaning that their activation and deactivation does not change the global FE connectivity. Upon activation, each FN is assigned a position in the element as well as a displacement value which is interpolated from standard nodes or already active FNs. Once activated, the FNs and the standard nodes are used to build sub-elements (SEs) in the A-FNM element which use standard element formulations to assemble the A-FNM element stiffness matrix. The A-FNM element uses two types of FNs (Fig. 1a) with specific roles and restrictions [48]:

- **Edge floating nodes:** An edge FN is connected to two different A-FNM elements and is restricted to be floating on a specific edge without being able to be positioned out of it upon activation. In this particular implementation, an interface and a position top/bottom are assigned to them upon activation to avoid incompatibilities.
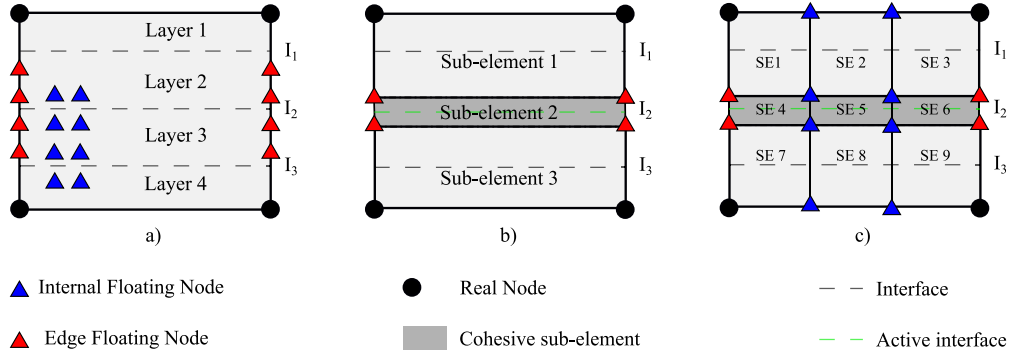
Fig. 1. (a) A 4-layer A-FNM element with 3 interfaces (I_n) initialized with 8 edge FNs and 8 internal FNs. (b) The A-FNM element with a cohesive sub-element in interface 2 (I_2). (c) The A-FNM element with interface I_2 refined with three cohesive sub-elements.
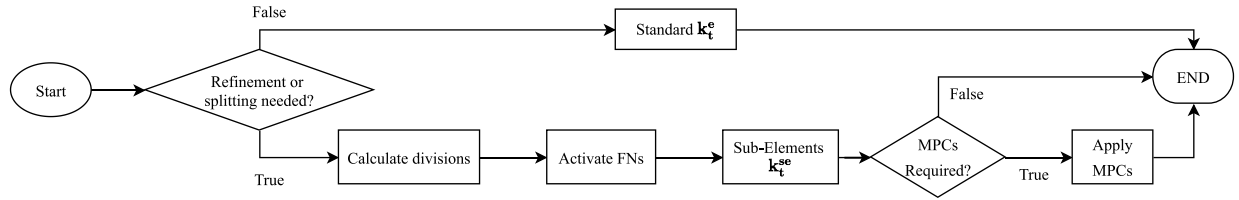

Fig. 2. A-FNM element tangent stiffness matrix k_t^e calculation.

• **Internal floating node**: Internal FNs are used to refine the element and have no restrictions apart from belonging to the A-FNM element they are assigned into.

The A-FNM element is initialized as a 4-node, n-layered element with $n-1$ interfaces as shown in Fig. 1a, for a 4 layers and 3 interfaces lay-up. This differs from the original A-FNM element from [50,52] where each A-FNM element may only contain 1 interface. During the analysis, the A-FNM element can be split with cohesive SEs in the interfaces (Fig. 1b) and refined with both cohesive and solid SEs (Fig. 1c). The element can be split in more than one interface, making it suitable for multiple delamination analysis with a single A-FNM element through the thickness.

The A-FNM element stiffness matrix is built in the sequence of operations shown in Fig. 2. If none of the interfaces requires to be refined nor split, a standard 4-node solid element subroutine is used to calculate the element tangent stiffness matrix $\mathbf{k_t^e}$. If any of the element interfaces requires a discretization change by means of splitting, refining or both at the same time, 4 operations are performed sequentially:

1. Calculate divisions
2. Activate FNs
3. Sub-element tangent stiffness matrix calculation
4. Application of Multi-Point Constraints (if needed)

Two types of divisions are needed depending on the refinement requirements: through the thickness of the laminate and longitudinal divisions along the interfaces. The number of through the thickness divisions (n_{thck}) is calculated based on the number of interfaces needing a discontinuity (n_{dsc}). In the case a refinement in the longitudinal direction of the element is needed, the number of longitudinal divisions (n_{lng}) is calculated. This depends on the cohesive sub-element length specified by the user (l_{coh}), which is translated into a number of cohesive sub-elements in the longitudinal direction per A-FNM element. Thus, n_{thck} and n_{lng} can be calculated as:

$$n_{thck} = 2 \cdot n_{dsc} - 1$$
$$n_{lng} = \lceil l_{el}/l_{coh} \rceil \qquad \text{If refinement is needed}$$
$$n_{lng} = 1 \qquad \text{If no refinement is needed}$$

where l_{el} is the length of the A-FNM element and $\lceil . \rceil$ is the ceiling function. The element divisions define a number of sub-elements n_{SE} as sown in Fig. 1b and c. A sub-element type is assigned to discern between cohesive and solid sub-elements.

After division, solid sub-elements are assigned a sub-laminate from the original full thickness laminate. Each sub-laminate contains the necessary lay-up information to assemble the layered sub-element tangent stiffness matrix. In Fig. 1c, for instance, SE1, SE2 and SE3 are assigned the same sub-laminate containing layers 1 and 2 whereas SE7, SE8 and SE9 are assigned a sub-laminate with layers 3 and 4.

Each sub-element uses different FNs that are activated when needed. Activating an FN requires assigning it a position and displacement [48], as well as including it in the internal A-FNM element connectivity, which relates FNs to sub-elements. Edge FNs are activated first as they are constrained by the neighbouring A-FNM elements. Interfaces which require the inclusion of a cohesive discretization are looped to check for active FNs in each edge of the element. If activation is needed, each edge FN is assigned a position in the interface (top/bottom) that ensures compatibility between A-FNM elements. An example is provided in Fig. 3 where A-FNM element 2 contains one active interface and shares FNs 5 and 6 with A-FNM element 1. FNs 7 and 8 are active in the same interface and are shared with A-FNM element 3. All FNs are assigned to Interface 2 with FNs 5 and 7 belonging to the top position while FNs 6 and 8 belonging to the bottom position, respectively. Without the top/bottom consideration, the same FN could be placed at the top surface of the interface for one A-FNM element and at the bottom of the same interface for a neighbouring A-FNM element, leading to inconsistency in the definition of crack opening directions. Initiation of the positions and current displacements of the newly activated edge FNs needs to be performed using interpolation between master nodes. Linear interpolation between the sub-laminate surrounding nodes is exemplified in Fig. 4 for Interface 1 (I_1) which uses nodes 1 & 5 and 4 & 9 as master nodes:

$$\begin{aligned} \mathbf{x_{7,8}} &= \mathbf{x_1} N_1 + \mathbf{x_5} N_5 & \mathbf{u_{7,8}} &= \mathbf{u_1} N_1 + \mathbf{u_5} N_5 \\ \mathbf{x_{11,12}} &= \mathbf{x_4} N_4 + \mathbf{x_9} N_9 & \mathbf{u_{11,12}} &= \mathbf{u_4} N_4 + \mathbf{u_9} N_9 \end{aligned} \qquad (1)$$

where N_i is the isoparametric shape function evaluated at node i.

The activation of the internal FNs is done only when a change in the internal refinement occurs. In such case all internal FN data is
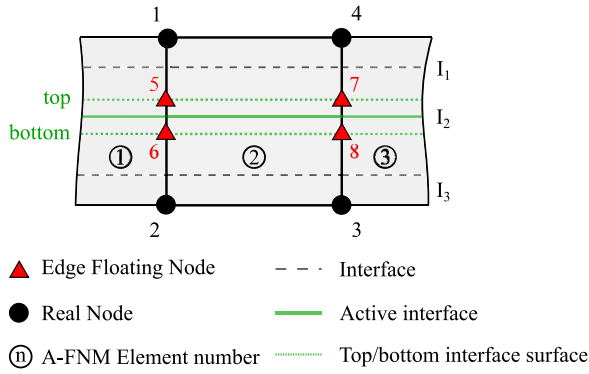
Fig. 3. Example of an A-FNM element (2) connected to two other A-FNM elements (1) and (3) with one active interface.
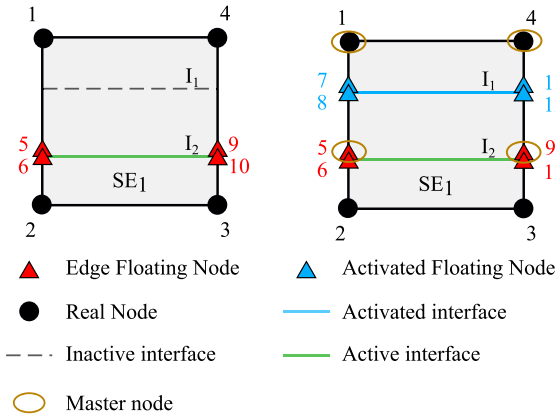

Fig. 4. Interface 1 (I_1) activation process from inactive (left) to active (right).

erased and all values are re-interpolated. The internal FNs are linearly interpolated similarly to the edge FNs using different interpolation nodes as exemplified in (Fig. 5):

$$
\begin{aligned}
x_{9,11} &= x_1 N_1 + x_4 N_4 & u_{9,11} &= u_1 N_1 + u_4 N_4 \\
x_{10,12} &= x_5 N_5 + x_7 N_7 & u_{10,12} &= u_5 N_5 + u_7 N_7 \\
x_{11,13} &= x_6 N_6 + x_8 N_8 & u_{11,13} &= u_6 N_6 + u_8 N_8 \\
x_{12,14} &= x_2 N_2 + x_3 N_3 & u_{12,14} &= u_2 N_2 + u_3 N_3
\end{aligned} \tag{2}
$$

where N_i is the isoparametric shape function of node i evaluated at the FN isoparametric position.

2.2. Multi-point constraint equations

In case an A-FNM element contains an interface which changes from active to inactive at one of its edges, as exemplified in Fig. 6a, an incompatibility may occur (Fig. 6b) as suggested in [48]. This incompatibility arises due to the FN being only active in one of the two elements sharing the edge. Multi-Point Constraint equations (MPC's) are applied to the FNs of the interface to correct the incompatibility as shown in Fig. 6c. The MPC's are defined using a master–slave approach re-using the interpolation scheme, in Eq. (1), which is also used for activation of the edge floating nodes.

2.3. Standard element formulations

Once the A-FNM element has been divided and active FNs defined, the sub-element tangent stiffness matrices k_t^{se} and internal force vectors f_{se} for implicit analysis are computed using standard FEA subroutines. These are subsequently assembled at the A-FNM element level to obtain

the A-FNM element tangent stiffness matrix k_t^e and the internal element force vector f_e, respectively.

Two finite elements have been formulated in this work adapting existing formulations: a 4-node cohesive element and a 4-node plane strain layered element with the possibility of an Enhanced Assumed Strains (EAS) formulation to avoid shear locking. The solid element follows the standard isoparametric formulation when the EAS formulation is deactivated.

The cohesive formulation applied in this work is based on [22,55] and adapted to a 2D zero-thickness 4-node cohesive element, referred to Coh4. Remark, different CZMs having more complicated mixed-mode cohesive laws, e.g. trilinear [56] and multilinear [23] CZ laws, could be implemented in the constitutive formulation of the CE subroutine without any modifications to the adaptive framework, i.e the ARS or the A-FNM element. A short outline of the Coh4 formulation is provided in the following for completeness. The interfacial constitutive model is based on a bilinear cohesive law, Fig. 7b, relating traction to separations. The critical energy release rate and onset traction are in general mode dependent and interpolated using a modified BK-criterion [22,57]. An updated Lagrangian formulation is employed in the Coh4 element, and the opening between crack faces of the element is decomposed into a mode I opening and mode II shearing component at the deformed mid surface between crack faces, see Fig. 7a, and interpolated using linear isoparametric shape functions. Numerical integration of the element tangent stiffness matrix and the internal force vector, respectively, is done by a 2-point Newton–Cotes integration scheme.

The 2D plane strain Enhanced Assumed Strains (EAS) equivalent single layer 4-node element, named EAS4 hereafter, uses a unique formulation adapted from the shell and solid-shell elements [53,54]. To the knowledge of the authors, the combination of formulations presented in this work is not available in literature for a 2-D case and thus, is outlined in the following. The EAS enhancement avoids shear locking on the unrefined areas of the model, while utilizing a layered element approach improves computational efficiency in multi-layered models.

In the EAS4 formulation, the compatible strains ε are enhanced with a second set of incompatible strains ε_{inc}:

$$
\varepsilon_{enh} = \varepsilon + \varepsilon_{inc} \tag{3}
$$

It is demonstrated in [53] that in order to obtain a stable element, the enhancing term of the strains needs to be calculated at the centre of the isoparametric space. This allows interpolating the strains in a geometry that is always a 1×1 square, but makes the element susceptible to distorted geometries. The enhanced strains at the centre of the element in the isoparametric space $\tilde{\varepsilon}_{inc}$ are calculated from 5 internal DOFs α using the matrix M [53]:

$$
\tilde{\varepsilon}_{inc} = M \alpha \quad \text{where} \quad M = \begin{bmatrix} r & 0 & 0 & 0 & rs \\ 0 & s & 0 & 0 & -rs \\ 0 & 0 & r & s & r^2 - s^2 \end{bmatrix} \tag{4}
$$

The transformation of the incompatible strains from the centre of the isoparametric space to any point of the element in the physical space (ε_{inc}) yields the $\tilde{M}$ matrix:

$$
\varepsilon_{inc} = \frac{|J_0|}{|J|} T_0^{-T} \tilde{\varepsilon}_{inc} \quad \Rightarrow \quad \tilde{M} = \frac{|J_0|}{|J|} T_0^{-T} M \tag{5}
$$

J and J_0 are the Jacobians of the isoparametric transformation at any point within the element and at the element centre, respectively. The quotient of the determinants of these Jacobians scales the strains, correcting for any difference in the element distortion at the centre and the current point. Notice that the transformation matrix T_0 transforms the enhanced strains from the isoparametric space to the physical space and is calculated from the terms in J_0:

$$
T_0 = \begin{bmatrix} J_{11}^2 & J_{21}J_{12} & 2J_{11}J_{12} \\ J_{12}J_{21} & J_{22}^2 & 2J_{21}J_{22} \\ J_{11}J_{21} & J_{12}J_{22} & (J_{11}J_{22} + J_{12}J_{21}) \end{bmatrix}_{r=s=0} \tag{6}
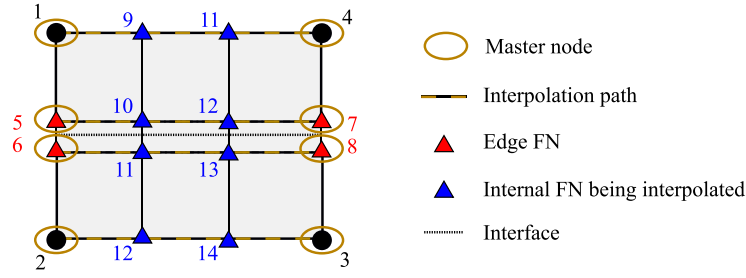$$

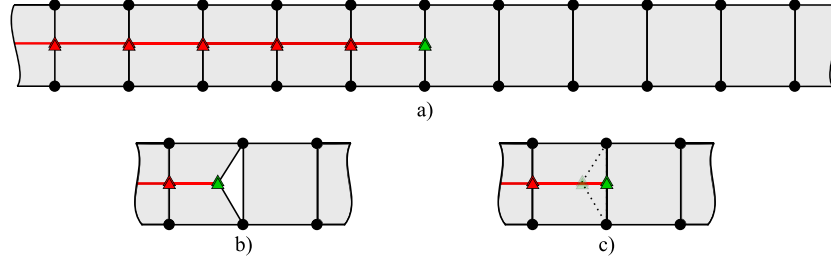**Fig. 5.** Interpolation for the internal FNs.

Fig. 6. (a) FNs that need MPCs are marked green. (b) Edge incompatibility created by the active/inactive interface transition. (c) Edge compatibility restored by enforcing MPC's. (For interpretation of the references to colour in this figure legend, the reader is referred to the web version of this article.)
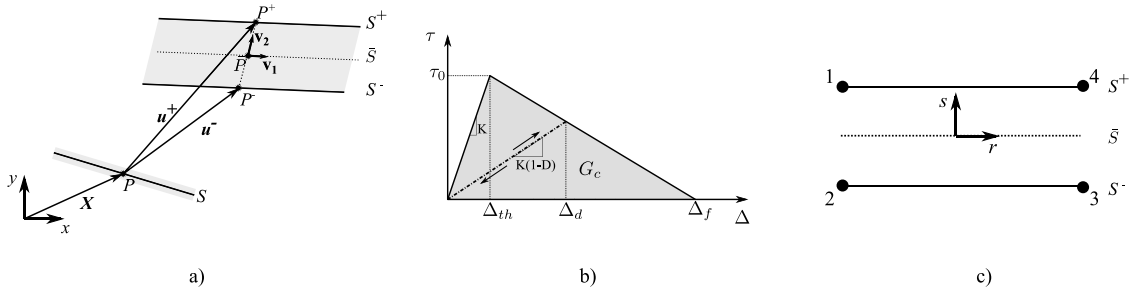

Fig. 7. (a) Representation of the kinematics of the deformed surface $\bar{S}$. (b) Bilinear cohesive law used in the formulation. (c) Cohesive element nodal numbering in the isoparametric space.

Following the variational formulation from [53], three stiffness sub-matrices are defined which lead to the sub-element stiffness matrix $\boldsymbol{k}_{se}$, obtained through static condensation of the internal degrees of freedom:

$$
\begin{aligned}
\boldsymbol{k}_{uu} &= \int_{se} \boldsymbol{B}^T \boldsymbol{C} \boldsymbol{B} \, dr \, ds \\
\boldsymbol{k}_{\alpha u} &= \int_{se} \tilde{\boldsymbol{M}}^T \boldsymbol{C} \boldsymbol{B} \, dr \, ds \quad \Rightarrow \quad \boldsymbol{k}_{se} = \boldsymbol{k}_{uu} - \boldsymbol{k}_{\alpha u}^T \boldsymbol{k}_{\alpha\alpha}^{-1} \boldsymbol{k}_{\alpha u} \\
\boldsymbol{k}_{\alpha\alpha} &= \int_{se} \tilde{\boldsymbol{M}}^T \boldsymbol{C} \tilde{\boldsymbol{M}}^T \, dr \, ds
\end{aligned}
\tag{7}
$$

where $\boldsymbol{B}$ is the standard isoparametric strain displacement matrix of a 2-D 4-Node solid element.

Numerical through the thickness integration is performed to calculate the expressions in Eq. (7) adapting the solid-shell formulation in [54] to 2D. Each layer is integrated using a full 2×2 Gauss quadrature. Two isoparametric mappings are needed (Fig. 8) to bring the integration limits of each layer to ± 1 and be able to perform numerical integration using Gauss Quadrature. The first isoparametric mapping is applied to all the nodes of the sub-element in a standard manner. The second isoparametric mapping is applied to each layer through a change of variable from s to t_l:

$$
s = -1 + \frac{1}{h}\left(2\sum_{i=1}^{l} h_i - h_l(1 - t_l)\right) \quad \Rightarrow \quad ds = \frac{h_l}{h} dt_l
\tag{8}
$$

where h_l is the thickness of the l'th layer and t_l is the isoparametric layer variable. The layer integration can be regarded as treating each layer as an element itself. The numerical integration of the element stiffness matrices from Eq. (7) at each layer is then carried out:

$$
\boldsymbol{k}_{uu}^l = \int_{-1}^{1}\int_{-1}^{1} \boldsymbol{B}^T \boldsymbol{C} \boldsymbol{B} \frac{h_l}{h} \, dr \, dt_l \approx \sum_{i=1}^{4} \boldsymbol{B}^T \boldsymbol{C} \boldsymbol{B} \frac{h_l}{h} |J|_i^l w_i
\tag{9}
$$

$$
\boldsymbol{k}_{\alpha u}^l = \int_{-1}^{1}\int_{-1}^{1} \tilde{\boldsymbol{M}}^T \boldsymbol{C} \boldsymbol{B} \frac{h_l}{h} \, dr \, dt_l \approx \sum_{i=1}^{4} \tilde{\boldsymbol{M}}^T \boldsymbol{C} \boldsymbol{B} \frac{h_l}{h} |J|_i^l w_i
\tag{10}
$$

$$
\boldsymbol{k}_{\alpha\alpha}^l = \int_{-1}^{1}\int_{-1}^{1} \tilde{\boldsymbol{M}}^T \boldsymbol{C} \tilde{\boldsymbol{M}}^T \frac{h_l}{h} \, dr \, dt_l \approx \sum_{i=1}^{4} \tilde{\boldsymbol{M}}^T \boldsymbol{C} \tilde{\boldsymbol{M}} \frac{h_l}{h} |J|_i^l w_i
\tag{11}
$$

where $|J|_i^l$ is the determinant of the standard isoparametric transformation Jacobian calculated at GP i of the layer l and w_i is the weight factor. The sub-element stiffness matrices $\boldsymbol{k}_{uu}$, $\boldsymbol{k}_{\alpha u}$ and $\boldsymbol{k}_{uu}$ are calculated by addition of the layer stiffness matrices:

$$
\boldsymbol{k}_{uu} = \sum_{l=1}^{L} \boldsymbol{k}_{uu}^l \qquad \boldsymbol{k}_{\alpha u} = \sum_{l=1}^{L} \boldsymbol{k}_{\alpha u}^l \qquad \boldsymbol{k}_{\alpha\alpha} = \sum_{l=1}^{L} \boldsymbol{k}_{\alpha\alpha}^l
\tag{12}
$$

where L is the total number of layers.

3. Adaptive refinement scheme for multiple cracks

An Adaptive Refinement Scheme (ARS) has been developed to continuously monitor and provide each interface of the A-FNM elements
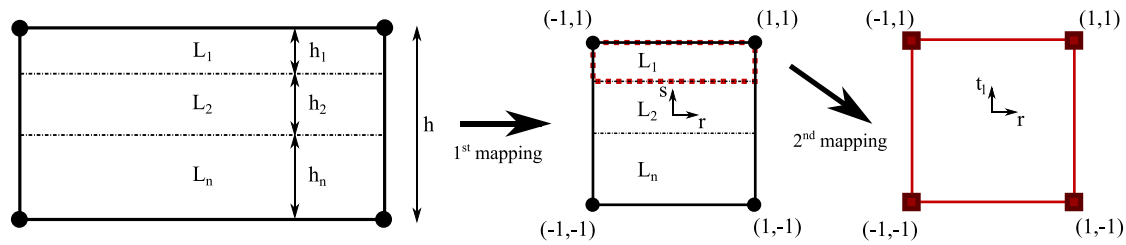
Fig. 8. Mappings used for the through the thickness numerical integration.

with a desired discretization throughout the analysis. The ARS is an essential novelty to model multiple delaminations with the aid of the A-FNM element presented in Section 2. The discretization is updated by the ARS at every iteration of the Newton–Raphson solver and is dependent on the CZ traction profile and current state of damage.

The traction profile in Fig. 9a may be classified into distinct zones depending on the traction value and its gradient. It has been demonstrated in [25,27–30] that a fine mesh containing 3–10 elements in the DPZ is necessary for accurate results and fast convergence. This mesh requirement ensures that the high gradient zone of the traction profile is correctly discretized. As it is also indicated in Fig. 9a, the position of the high gradient zone of the traction profile and its extension for a given crack tip is determined by the extension of the DPZ, which is defined as the length where $d \in \,]0,1[$. Remark, that in this work crack tip refers to the onset of damage point as shown in Fig. 9. In a general delamination problem, the DPZ length may vary during the course of the analysis due to variations in geometry, material, and loading conditions. Thus, to accurately track the position of the high gradient zone of the traction profile, the cohesive damage variable, d, is defined as the main driver within the ARS. The cohesive damage variable is readily available during the analysis without the need of additional post-processing steps, making it desirable for computational efficiency. Notice that a small part of the high gradient traction zone, which still needs a fine discretization, falls out of the DPZ just before the coarse zone begins.

The traction profile in Fig. 9a can be split into four zones defined by the damage variable d and the expected traction gradients associated with it. Discretization of each zone is done separately to ensure accurate results and convergence, and defined by the following four states:

- **Full damage state:** The fully damaged zone ($d = 1$) is discretized with fully damaged coarse cohesive elements to avoid interpenetration of the crack faces.
- **Refined state:** The ongoing damage and high traction gradient zone ($1 > d \geq 0$) is modelled with a fine mesh of active cohesive elements.
- **Coarse state:** The undamaged ($d = 0$) and low gradient zone of the traction profile is modelled with coarse undamaged cohesive elements to capture the stored elastic energy, which is important for smooth and accurate results during the ARS adaptive updates.
- **Idle state:** The undamaged ($d = 0$) and very low gradient zone of the traction profile is considered inactive and thus does not require cohesive elements.

ARS provides each interface in each A-FNM element with a single refinement state as illustrated in Fig. 9b. In a multiple delamination case, two delamination cracks may enter in the same interface within an A-FNM element and thus provide two refinement states for the same interface. In such an event, the following refinement hierarchy is defined to select the proper discretization of the interface in the A-FNM element: Full damage >Refined >Coarse >Idle. Please notice that a multiple delamination case may also include delaminations at several interfaces within the same A-FNM element. In such case, the refinement planning is done at the A-FNM element level, described in Section 2,

by selecting the longitudinal A-FNM element divisions (n_{lng}) according to the most refined interface included in the A-FNM element.

The sole user input for the ARS algorithm is the coarse discretization length (l_{cor}) for the low gradient zone of the traction profile. This discretization length is set prior to execution of the analysis and may be set conservatively as it has little impact on the computational cost. During the analysis the ARS algorithm makes use of the following definitions, i.e. internal logical variables, at the A-FNM Element Interface (EI) level:

- **Interface in the DPZ:** An interface is in the DPZ if any of its integration points has a damage value between 0 and 1 ($d \in \,]0,1[$).
- **Damaged interface:** An interface in the element is damaged when all its integration points have damage values of 1 ($d = 1$).
- **Crack tip interface:** An interface contains a crack tip when an integration point is undamaged ($d = 0$) and others are partly or fully damaged ($0 < d \leq 1$).

The main actions of the ARS algorithm are shown in Fig. 10. The output of the algorithm is the interface refinement states for all interfaces in all A-FNM elements of the model. Initially, the algorithm saves the current EI states of the model Fig. 11a and resets all EI states to Idle state Fig. 11b. A succession of operations is then performed for each interface in the model defined by the layup of the analysed laminate (interface loop). All crack tips in the interface are determined by looping the active cohesive sub-elements of the interface. For each crack tip, the EI states in the DPZ and its immediate EI neighbour are set to a Refined state Fig. 11c. EIs within the user defined length, l_{cor}, measured from the uttermost refined element, are set to Coarse state Fig. 11d. To improve convergence and reduce oscillations of the adaptive refinement, EIs that have been set to a Refined state cannot revert to a Coarse or Idle state during the equilibrium iterations of the Newton–Raphson solver Fig. 11e. This condition avoids EIs oscillating between refined and non-refined states when the DPZ enters a new EI. Remark that the condition only prevails within the equilibrium iteration loop of the Newton–Raphson solver and is reset at every new solution step.

4. Simulation studies

The presented formulation has been implemented in a Matlab FEA code which uses ANSYS Mechanical 2020 R2 for preprocessing, i.e. define geometry, material properties, layup, boundary conditions, and mesh. Addition of the pre-cracks, FNs and specific formulation parameters is done in a second pre-processing phase in Matlab. The analysis is executed in Matlab using a displacement controlled Newton–Raphson solution method to trace the nonlinear softening equilibrium path during progressive advancement of single or multiple delaminations. A separate, but equivalent, Matlab implementation using the base element technologies presented in Section 2.3 without adaptive refinement and FNM is used as reference for assessing the performance and accuracy of the adaptive formulation. This section presents three groups of results. Firstly, simulations of the standard double cantilever beam (DCB) specimen, end notched flexure (ENF) specimen, and mixed mode bending (MMB) specimen are conducted to verify the implementation and prove the accuracy and computational efficiency of
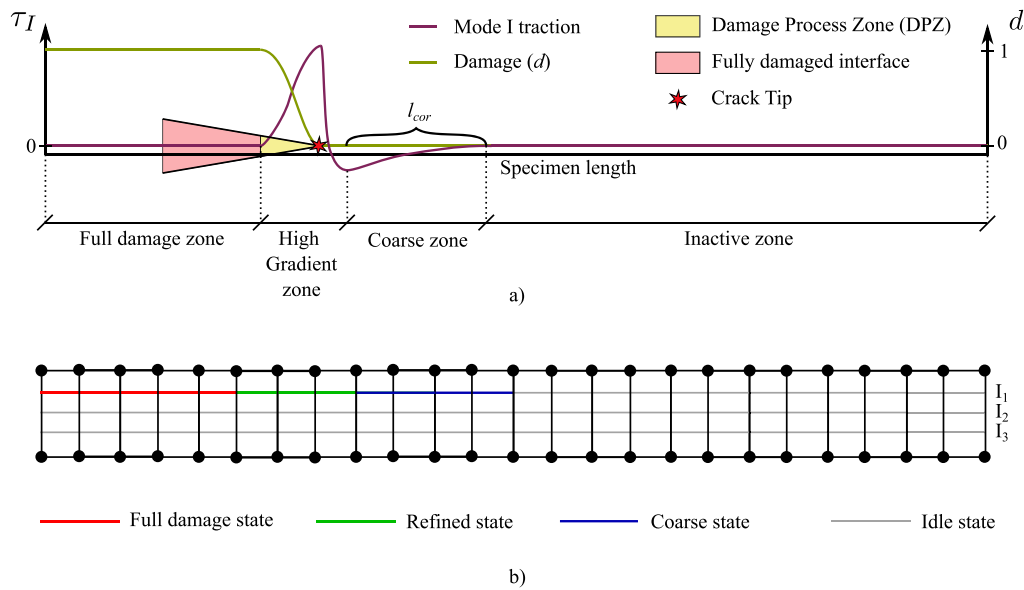
Fig. 9. (a) Traction profile, in purple, induced by the damage state, in green, with the 4 proposed classification zones. (b) Example of refinement states for a specimen with three interfaces of which only the first interface is delaminating. (For interpretation of the references to colour in this figure legend, the reader is referred to the web version of this article.)
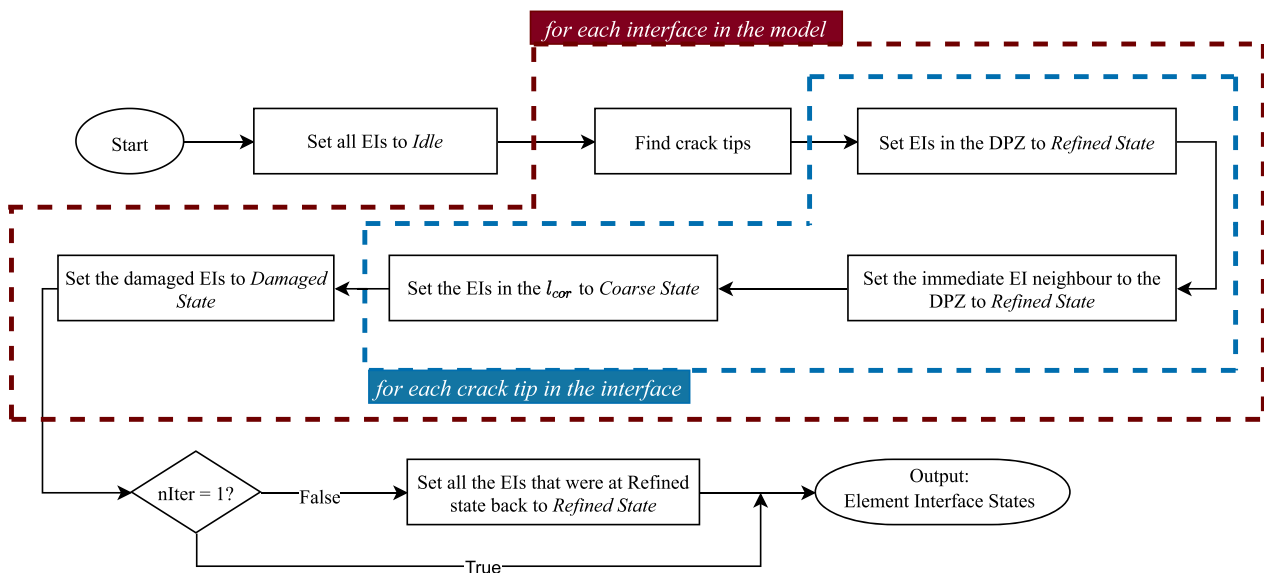

Fig. 10. Flowchart of the adaptive refinement scheme algorithm executed at every equilibrium iteration in the Newton–Raphson solver.

the formulation on well-known examples. Secondly, three simulation studies are presented to demonstrate the unique capabilities of the adaptive refinement scheme formulation: A simulation of a case with varying length of the damage process zone as the crack progress and two simulations featuring multiple delaminations. Finally, parametric studies demonstrate that the coarse discretization length (l_{cor}), is the only discretization variable affecting the results as long as the cohesive sub-element length (l_{coh}) is kept at a reasonable value meaning that 3–10 CEs are placed in the DPZ.

4.1. Validation and verification

Validation of methods and verification of the implementation is conducted by performing a simulation of DCB, ENF, and MMB tests which are performed using the geometry and boundary conditions shown in Fig. 14 and the material properties stated in Table 1. A two layer unidirectional layup (0, 0) is used in the three analyses. For

the MMB test, the lever is modelled using MPCs. Mesh size related parameters for the models are stated in Table 2 together with the user defined coarse discretization length, l_{cor}, needed for the ARS. The chosen cohesive sub-element length l_{coh}, is selected to provide accurate results and fast convergence rates in both the adaptive FE implementation, which makes use of the A-FNM element and the ARS, and the reference FE implementation and provides a minimum of 10 cohesive elements in the DPZ throughout the analysis. The DPZ length obtained in the DCB and ENF analysis is approximately 0.923 mm and 4.210 mm, respectively. The reference FE models are defined using standard element formulations, i.e., Coh4 and EAS4 elements, and identical mesh parameters and material definitions as the models simulated using the adaptive framework. Note that the EAS stabilization of the 2D solid elements is only utilized for the coarse solid mesh and deactivated for the fine solid mesh. Pre-cracked areas of the reference FE models are meshed using the element size used in the adaptive refinement cases for direct comparison, resulting in the mesh in Fig. 13. It is assumed that
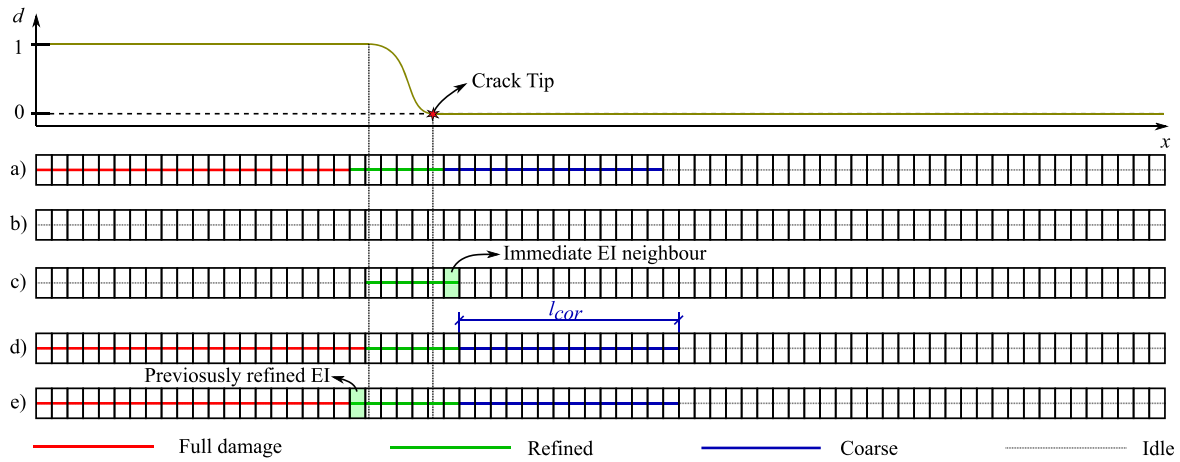
Fig. 11. Application of the ARS algorithm for the traction profile on top from the existing interface states (a) to the outputted element interface states (e) for $n_{iter} > 1$.

Fig. 12. Basic A-FNM element mesh used in the analyses. Remark that the thickness of the specimen varies for some of the numerical tests.

Fig. 13. Mesh of the reference model used for the performance and accuracy comparisons. Remark that the thickness of the specimen varies for some of the numerical tests.
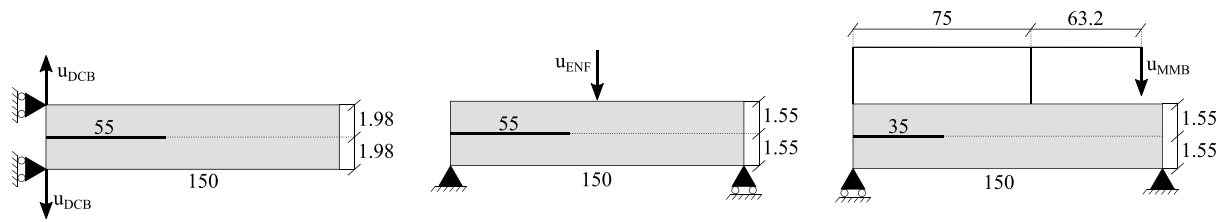

Fig. 14. Geometry and boundary conditions for the DCB (left), ENF (middle) and MMB (right) tests. Dimensions are stated in [mm].

Table 1
Material properties for the DCB, ENF and multiple delamination numerical tests.
Source: Penalty stiffness K_0 taken from [26]

	DCB [25]	ENF/MMB [58]	Mult. Delam. [20]
E_{11}	150 [GPa]	120 [GPa]	115 [GPa]
$E_{22} = E_{33}$	11 [GPa]	10.5 [GPa]	8.5 [GPa]
$\nu_{12} = \nu_{13}$	0.45	0.5	0.29
ν_{23}	0.25	0.3	0.3
$G_{12} = G_{13}$	6 [GPa]	5.25 [GPa]	4.5 [GPa]
G_{23}	3.7 [GPa]	3.48 [GPa]	4.5 [GPa]
G_I	352 $[\frac{J}{m^2}]$	260 $[\frac{J}{m^2}]$	330 $[\frac{J}{m^2}]$
G_{II}	1000 $[\frac{J}{m^2}]$	1002 $[\frac{J}{m^2}]$	800 $[\frac{J}{m^2}]$
τ_{I0}	60 [MPa]	30 [MPa]	16.5 [MPa]
τ_{II0}	–	58.9 [MPa]	35 [MPa]
η	–	2	2
K_0	5.55e14 $[\frac{N}{mm^3}]$	5.55e14 $[\frac{N}{mm^3}]$	5.55e14 $[\frac{N}{mm^3}]$

the user does not have previous knowledge of the final crack extension and location meaning that the reference model refinement spans the entire potential crack path.

Load–displacement curves for the three numerical tests are shown in Fig. 15. Agreement between the reference FEA implementation and the adaptive implementation is perfect and no jumps or oscillations in the response plots may be observed as the mesh refinement adaptively occurs during the analyses. The speedup using the adaptive implementation is reported in Table 3 based on CPU time to avoid influence from parallel execution of the FEA codes. Reported CPU times are average times obtained from 4 executions of each numerical test. The speedup of the adaptive FEA implementation compared to the reference is a factor of 4–5.5 for the simulated cases. The speedup is expected to increase dramatically for larger models, i.e., geometry and laminate layers, as the number of DOFs would increase substantially for the reference FEA implementation compared to the adaptive implementation, which still would exploit a coarse discretization in most of the model. This statement is supported by a DCB numerical test performed with a specimen of the same thickness as the one shown in Fig. 14 but 10 times longer, reaching a total length of 1.5 m. The same material for the DCB test shown in Table 1 is used together with the same ARS and mesh parameters listed in Table 2. This test resulted in a speedup factor of 93 with respect to a simulation in the reference model with an equally long DCB specimen and equivalent mesh characteristics.
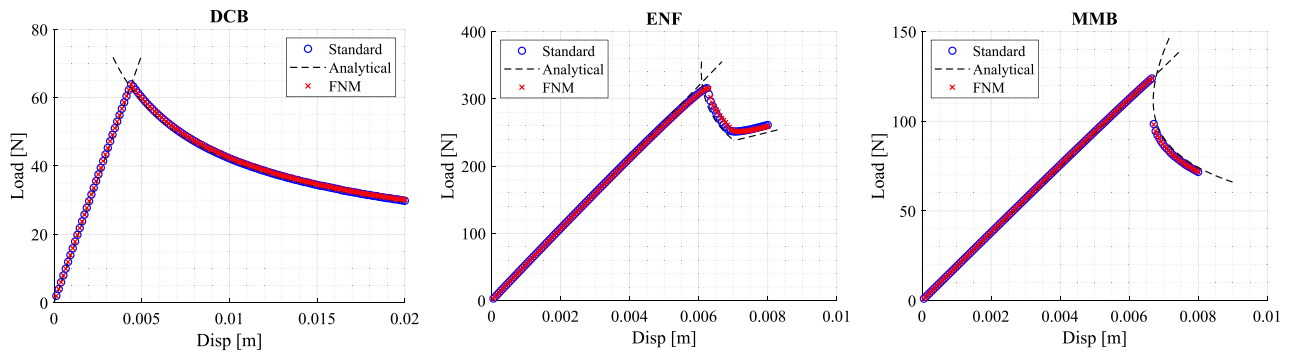
Fig. 15. Comparison between the reference and the adaptive formulation for the DCB, ENF and MMB tests. Analytical solution extracted from the ASTM standard [59].

Table 2
Mesh parameters and ARS l_{cor} parameter used in the DCB, ENF and MMB numerical tests.

Parameter [mm]	DCB	ENF	MMB
Cohesive elem. length l_{coh}	0.119	0.208	0.104
A-FNM elem. length	1.66	1.66	1.66
ARS l_{cor} parameter	6.66	6.66	6.66

Table 3
Comparison of the computational performance between the reference and the adaptive formulation.

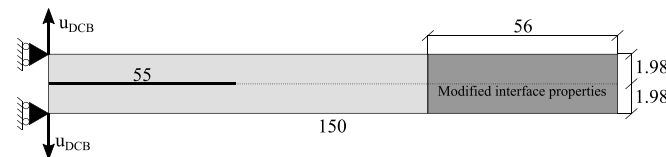| CPU Time [s]	DCB	ENF	MMB	Double	Triple
Reference	2099	2603	13597	39483	678410
A-FNM	394	604	3251	3691	48984
Speed-up	5.32	4.30	4.18	10.6	13.84

Fig. 16. DCB test with an abrupt change of interfacial properties.

4.2. Formulation capabilities

To demonstrate the adaptive capabilities of the A-FNM element formulation and ARS a case is considered in which the DPZ length varies as the crack propagates. Furthermore, two cases with multiple delaminations propagating simultaneously are presented: a double and a triple delamination model.

4.2.1. Damage process zone length change

The length of a DPZ may vary during delamination propagation due to many factors such as variations in geometry, constitutive and interfacial properties, and mode-mixity. To verify that the adaptive formulation can successfully tackle changes in length of the DPZ during simulation an artificial DCB is analysed. The definition of the DCB model is identical to that studied in Section 4.1 except the cohesive properties of the dark grey region marked in Fig. 16, which are set to $G_I = 1000$ J/m^2 and $\tau_I = 10$ MPa enlarging the DPZ in this region. Simulated response curves from the reference and adaptive implementation, respectively, are shown in Fig. 17. The sudden enlargement of the DPZ is captured accurately by the ARS. From the initial state (o) the ARS enforces a minimal refinement as the DPZ grows until the maximum load level at the first limit point (A). The delamination crack then propagates (softening) with a constant DPZ length until it reaches the section with reinforced interfacial properties (B). Next, the response

reverts to hardening as the DPZ grows until fully developed at the second limit point (C). Again, a softening response is encountered as the delamination crack propagates in the reinforced interface (D). The ARS adequately captures the variations in the DPZ during the execution of the analysis.

4.2.2. Double delamination

A multiple delamination numerical test has been performed following the benchmarking in [20]. The geometry of the test specimen, which features a second delamination, is shown in Fig. 18. The material used is slightly modified following [26] to obtain traction profiles from a more realistic material than the one in [20], where low onset stresses are used to enlarge the DPZ. The analysis is performed with the same coarse mesh of 90 elements as the one used in the previous analysis Fig. 12. A cohesive element size (l_{coh}) of 0.11 mm is chosen and the length of the coarse mesh (l_{cor}) is kept at 6.66 mm.

Simulated results in Fig. 19 show almost perfect agreement between the reference and the adaptive implementation. In the first stage of the analysis, after reaching the first limit point, delamination propagation only occurs in the first interface at crack tip ①, marked in Fig. 19. When the propagating crack tip ① reaches the position of crack tip ② very unstable crack propagation of crack tip ① takes place resulting in a deflection limit point in the equilibrium curve. During the unstable growth, crack tip ① surpasses crack tip ② (A) and onsets the second delamination at crack tip ③. A second nearly linear loading path until the limit point (B) is a consequence of further propagation of crack tip ① while a second DPZ is formed at crack tip ③. Hereafter a softening response is caused by combined delamination propagation at interface 1 and 2 at respectively crack tip ① and ③. By considering the final deformed shape and associated mesh in Fig. 21 (C), it is clear that the ARS algorithm conforms perfectly to the three different DPZ lengths in the problem. A short refinement zone covering two A-FNM elements is observed at crack tip ② since the DPZ here is not fully developed. At crack tip ①, a fully developed but relatively short DPZ is encountered since delamination propagation is due to peeling off a thin layer with low bending stiffness and thus only needs a refinement zone three A-FNM elements long. Finally, a larger DPZ is encountered at crack tip ③ due to thicker and thus stiffer adjacent sub-laminates, which is captured by a refinement zone covering four A-FNM elements. The performance comparison between the adaptive formulation and the reference model is stated in Table 3 under the name "Double".

4.2.3. Triple delamination

A case displaying three delaminations is defined with the geometry and boundary conditions shown in Fig. 20. The test case is a further extension of the double delamination case by adding a third initial crack. The same material and mesh properties, including the ARS user parameter l_{cor}, from the double delamination test are applied.

Results from reference FEA and using the adaptive FNM formulation are shown in Fig. 21, and again the adaptive FNM formulation provides
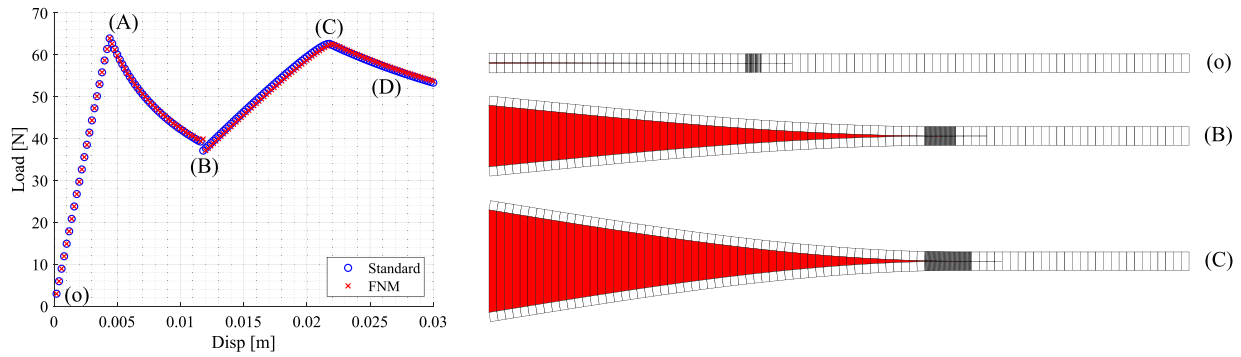
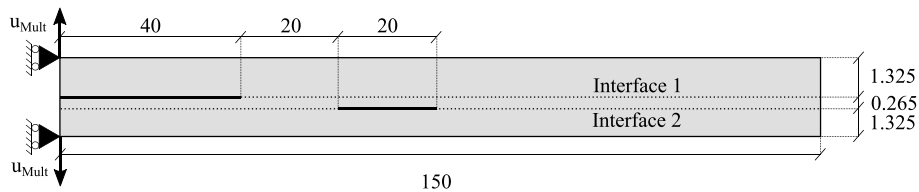**Fig. 17.** Load–displacement equilibrium curves for test case with varying DPZ length.

Fig. 18. Geometry and boundary conditions for the double delamination test.
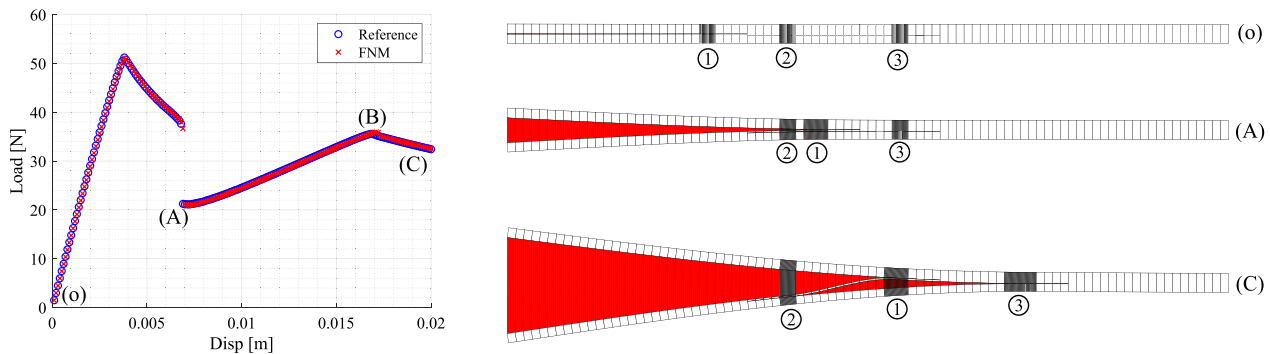

Fig. 19. Left: Double delamination load displacement curve. Right: Deformed shape at three stages of the analysis.
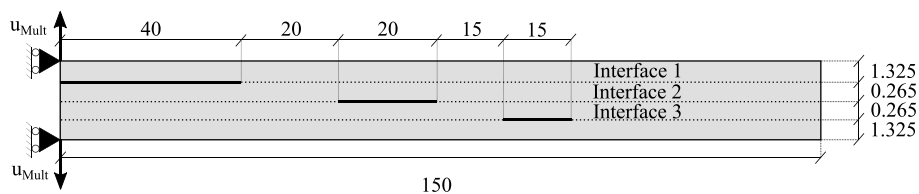

Fig. 20. Geometry and boundary conditions for the triple delamination test.

accurate results. Due to the presence of a third delamination, and thus a total of five crack tips, which results in a more compliant structure, the final propagation phase from point (B) is delayed. This test case further demonstrates the robustness of the adaptive formulation being that it can deal with several DPZs of different and varying lengths while being computationally effective since it is based on an initial equivalent single-layered coarse mesh. The performance comparison between the adaptive formulation and the reference model is stated in Table 3 under the name "Triple".

4.3. Parametric studies of key ARS and mesh parameters

To test the robustness and generality of the ARS algorithm embedded in the adaptive implementation a set of parametric studies are conducted by varying key parameters influencing the adaptive

refinement. The parameters studied are the user inputted coarse discretization length (l_{cor}), the length of the refined area, and the refined cohesive sub-element element length (l_{coh}) defined by the user. Albeit the initial A-FNM element mesh size and the cohesive element length parameter may be argued not to be specific parameters related to ARS they are included for completeness. The parametric studies are conducted on the DCB (mode I) and ENF (mode II) examples from Section 4.1 by varying the aforementioned four parameters from their base values. At first, the internally fixed extra refinement length in front of an identified crack tip, which through the ARS refines a single neighbouring element to the element containing the crack tip (Section 3), is studied. This means studying the effect of increasing the number of elements that are refined by increasing the refinement length ARS internal variable. The results of the parametric study are shown in Figs. 22a and 22b, and by considering that the coarse A-FNM element
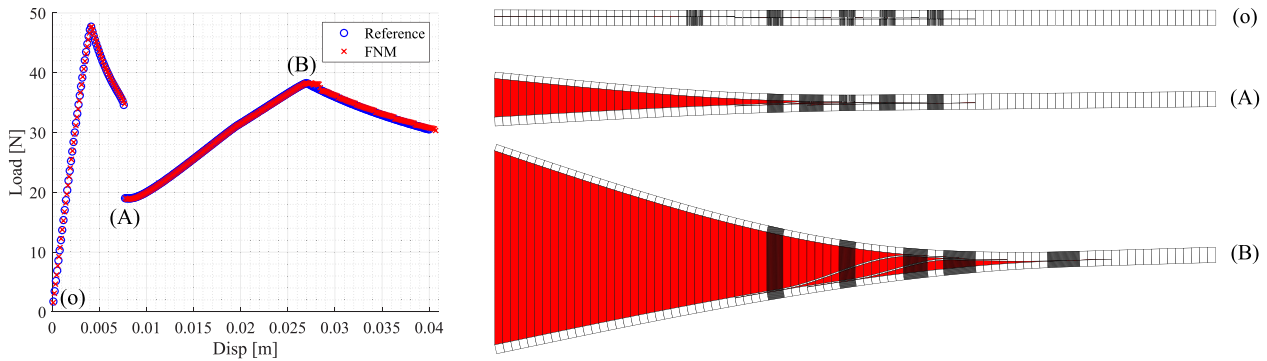
Fig. 21. Left: Triple delamination load displacement curve. Right: Deformed shape at three stages of the analysis.

(a) DCB numerical test
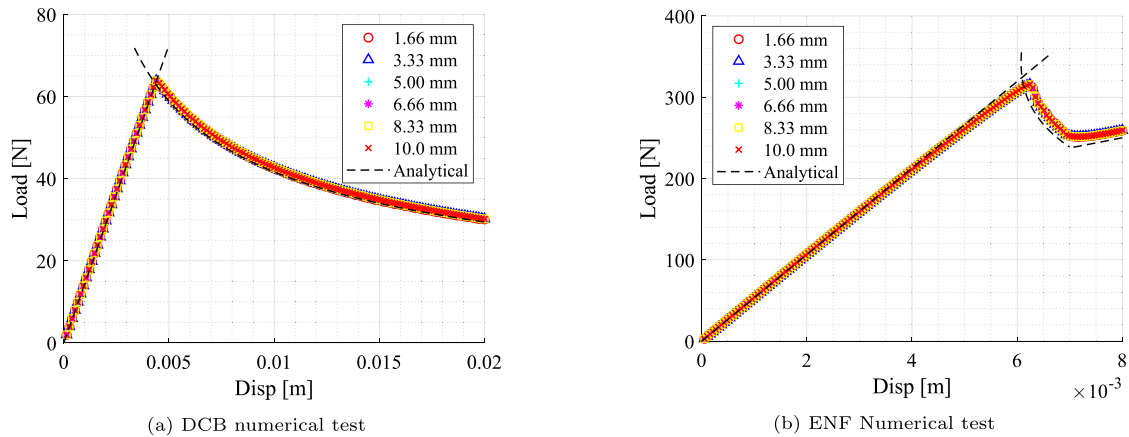
(b) ENF Numerical test

Fig. 22. Effect of changing the size of the refined area in front of the crack tip. Analytical solution extracted from the ASTM standard [59].

length is 1.66 mm, it may be observed that further refinement than the first A-FNM element neighbour is unnecessary. In Figs. 23a and 23b results from varying the user inputted coarse discretization length are shown. The base value for $l_{cor} = 6.66$ mm, which corresponds to four A-FNM elements, has been varied to cover 1–6 A-FNM elements. The aim of the coarse discretization is the insertion of coarse undamaged cohesive elements to capture the stored elastic energy ahead of the DPZ, refer to definition in Section 3. As may be observed in Figs. 23a and 23b a too coarse discretization length may lead to erroneous and oscillating equilibrium solutions, which also results in increased computational time due to the additional iterations needed by the solver for reaching equilibrium. A coarse discretization length of 10 times the expected size of the DPZ seems appropriate. However, a conservative large value for the coarse discretization length may be inputted as it has little impact on the computational cost since it just adds a few DOFs when inserting cohesive elements in the coarse discretization. The robustness of the ARS algorithm concerning discretization of the initial coarse mesh of A-FNM elements is tested and results are reported in Figs. 24a and 24b. From the baseline mesh with an element size of 1.66 mm, the initial mesh size has both been increased and decreased with a factor of two and four, respectively. As demonstrated in the response plots the ARS implemented in the adaptive formulation is unaffected by the initial mesh size. However, a too coarse initial mesh would cause inaccuracies in representing the correct deformation state of the non-refined regions of the structure despite the use of an EAS formulation within the solid elements. Finally, a study is conducted to demonstrate that the ARS is insensitive to the cohesive element size (l_{coh}) of the refined regions. Considering that the length of the DPZ for the DCB and ENF example approximately is 0.923 mm and 4.210 mm, respectively, the cohesive element length (l_{coh}) has been varied providing 3–9 cohesive elements within the DPZ for the DCB numerical test and 10–35 cohesive elements for the ENF case. The results of this study are presented in Figs. 25a

and 25b, and confirm that as long the rule of thumb is followed by discretizing the DPZ with 3–10 elements, accurate results and good convergence properties are achieved.

5. Conclusions

In the present paper, a new formulation for efficient simulation of multiple delamination crack growth under static loading in laminated composites is presented. The formulation relies on an Adaptive Floating Node Method adaptive element (A-FNM) and an Adaptive Refinement Scheme (ARS). The A-FNM element is capable of efficiently splitting, refining and coarsen itself adaptively during the analysis without modifying the global model connectivity, while maintaining model compatibility through auto-generated multi-point constraint equations. The underlying finite element formulations used by the A-FNM element are a linear cohesive element and a 4-noded plane strain EAS layered element (EAS4) allowing an initial coarse mesh of A-FNM elements while ensuring accurate results.

The adaptive refinement of the A-FNM element is driven by the ARS, which during analysis adaptively updates the A-FNM element interface discretizations ensuring accurate results, fast convergence and low solution times. The ARS algorithm only requires a single user input (l_{cor}) and solely relies on the cohesive damage variable, d, to assess the discretization needs in each interface of the model. The A-FNM element single user input is the cohesive element length l_{coh}, which may be set in accordance with traditional guidelines proposed for standard delamination analysis using cohesive elements. Remark, that l_{coh} could automatically and adaptively be defined by tracking the current DPZ length at every converged substep and using the guidelines proposed in [25,27–30] to ensure a certain number of CEs discretize the DPZ.

Numerical studies of standard DCB, ENF and MMB analysis cases utilizing the ARS and the A-FNM element prove the validity and
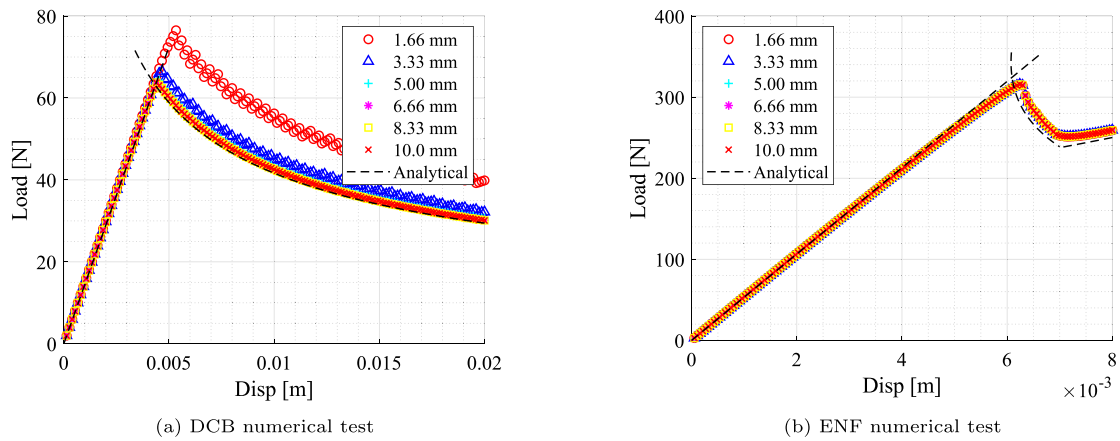
(a) DCB numerical test

(b) ENF numerical test

Fig. 23. Effect of changing the coarse discretization length l_{cor}. Analytical solution extracted from the ASTM standard [59].

(a) DCB numerical test
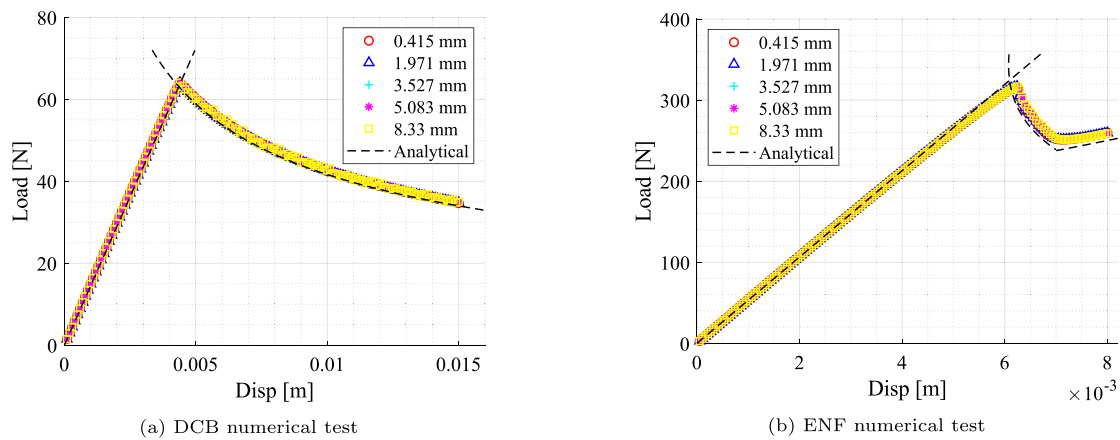
(b) ENF numerical test

Fig. 24. Effect of changing the size of the A-FNM elements in the initial coarse mesh (Fig. 12). Analytical solution extracted from the ASTM standard [59].
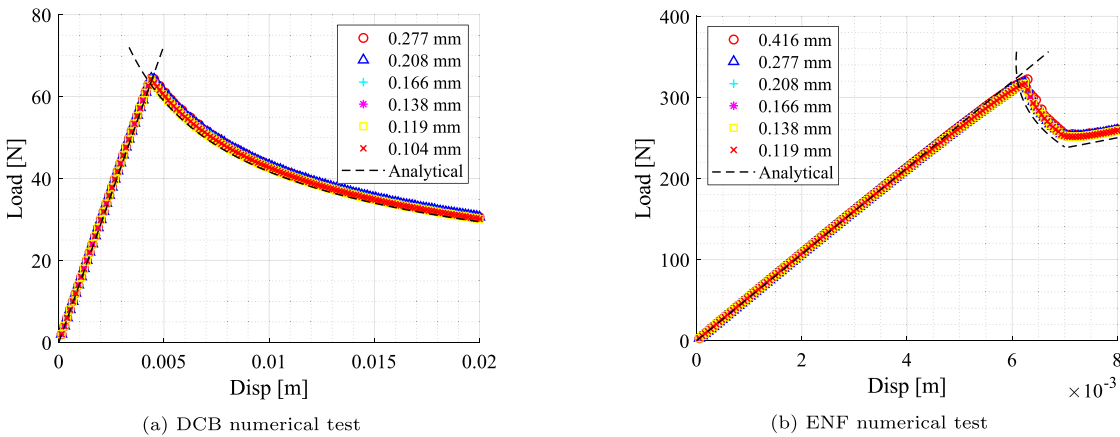

(a) DCB numerical test

(b) ENF numerical test

Fig. 25. Effect of changing the cohesive sub-element size l_{coh}. Analytical solution extracted from the ASTM standard [59].

accuracy of the formulation while decreasing the computational time by a factor of 4 to 5. Furthermore, it is expected that for larger finite element models having cohesive interfaces speedups of hundreds or even higher can be achieved. More advanced numerical cases involving an abrupt change of interfacial properties in a DCB specimen as well as double and triple delamination cases demonstrate the generality of the formulation. The accurate results obtained on these advanced cases prove that the presented formulation can adaptively refine, coarsen, split, and insert cohesive elements when needed during the analysis of general multiple delamination growth models having varying DPZ

lengths. Speedups of 10.6 and 13.84 were achieved for double and triple multiple delamination cases.

The robustness and accuracy of the presented formulation are verified by parametric studies of key ARS and mesh parameters and clearly show that the user input coarse discretization length, l_{cor}, is the sole mesh related parameter affecting the accuracy, given a sufficient small l_{coh} is chosen, while its impact on computational cost is very limited. It is therefore recommended to set this parameter conservatively large according to the expected size of the DPZ. Natural future extensions of the adaptive framework would be to expand it to 3D FEA and include

damage onset for delaminations. Both extensions would increase the complexity of both ARS and the A-FNM element, but the authors do not foresee any unsolvable problem in that regard.

The presented formulation is a step towards real-life engineering simulation and design purposes involving progressive delamination in larger composite structures. The A-FNM and ARS combination presented in this work provides the same accuracy as traditional FEA models having cohesive interfaces but at a fraction of the computational cost since potential crack paths do not need to be defined and discretized prior to executing the analysis.

CRediT authorship contribution statement

Guillem Gall Trabal: Conceptualization, Methodology, Software, Validation, Visualization, Investigation, Writing – original draft, Writing – review & editing. **Brian Lau Verndal Bak:** Supervision, Conceptualization, Methodology, Writing – review & editing, Funding acquisition. **Boyang Chen:** Supervision, Conceptualization, Methodology, Writing – review & editing. **Esben Lindgaard:** Supervision, Conceptualization, Methodology, Writing – review & editing, Funding acquisition.

Declaration of competing interest

The authors declare that they have no known competing financial interests or personal relationships that could have appeared to influence the work reported in this paper.

Acknowledgements

References

[1] Tabiei A, Zhang W. Composite laminate delamination simulation and experiment: A review of recent development. Appl Mech Rev 2018;70(3):030801. http://dx.doi.org/10.1115/1.4040448.

[2] Griffits AA. The phenomena of rupture and flow in solids. Philos Trans R Soc Lond 1920;A(221):163–98.

[3] Irwin G. Analysis of stresses and strains near the end of a crack traversing a plate. J Appl Mech 1957;24:361–4. http://dx.doi.org/10.1115/1.4011547.

[4] Krueger R. Virtual crack closure technique: history, approach, and applications. Appl Mech Rev 2004;57(2):109–43.

[5] Rice JR. A path independent integral and the approximate analysis of strain concentration by notches and cracks. J Appl Mech Trans ASME 1964;35(2):379–88. http://dx.doi.org/10.1115/1.3601206.

[6] Lee L, Tu D. J integral for delaminated composite laminates. Compos Sci Technol 1993;47(2):185–92. http://dx.doi.org/10.1016/0266-3538(93)90046-J.

[7] Dugdale DS. Yielding of steel sheets containing slits. J Mech Phys Solids 1960;8(2):100–4.

[8] Barenblatt GI, et al. The mathematical theory of equilibrium cracks in brittle fracture. Adv Appl Mech 1962;7(1):55–129.

[9] Hillerborg A, Modéer M, Petersson. Analysis of crack formation and crack growth in concrete by means of fracture mechanics and finite elements. Cem Concr Res 1976;6(6):773–81.

[10] Carreras L, Bak B, Turon A, Renart J, Lindgaard E. Point-wise evaluation of the growth driving direction for arbitrarily shaped delamination fronts using cohesive elements. Eur J Mech A Solids 2018;72:464–82. http://dx.doi.org/10.1016/j.euromechsol.2018.05.006.

[11] Carreras L, Lindgaard E, Renart J, Bak B, Turon A. An evaluation of mode-decomposed energy release rates for arbitrarily shaped delamination fronts using cohesive elements. Comput Methods Appl Mech Engrg 2019;347:218–37. http://dx.doi.org/10.1016/j.cma.2018.12.027.

[12] Bfer G. An isoparametric joint/interface element for finite element analysis. Internat J Numer Methods Engrg 1985;21(4):585–600.

[13] Gens A, Carol I, Alonso E. An interface element formulation for the analysis of soil-reinforcement interaction. Comput Geotech 1989;7(1–2):133–51.

[14] Schellekens H, De Borst R. Geometrically and physically non-linear interface elements in finite element analysis of layered composite structures. In: Developments in the science and technology of composite materials. Springer; 1990, p. 749–54.

[15] Mi Y, Crisfield MA, Davies GAO. Progressive delamination using interface elements. J Compos Mater 1997;32(14(1998)):1246–72.

[16] ans M. Crisfield JC, Kinloch A, Busso E, Matthews F, Qiu Y. Predicting progressive delamination of composite material specimens via interface elements. Mech Compos Mater Struct 1999;6(4):301–17.

[17] Ortiz M, Pandolfi A. Finite-deformation irreversible cohesive elements for three-dimensional crack-propagation analysis. Internat J Numer Methods Engrg 1999;44(9):1267–82.

[18] De-Andrés A, Pérez J, Ortiz M. Elastoplastic finite element analysis of three-dimensional fatigue crack growth in aluminum shafts subjected to axial loading. Int J Solids Struct 1999;36(15):2231–58.

[19] Chowdhury SR, Narasimhan R. A cohesive finite element formulation for modelling fracture and delamination in solids. Sadhana 2000;25(6):561–87.

[20] Alfano G, Crisfield MA. Finite element interface models for the delamination analysis of laminated composites: Mechanical and computational issues. Internat J Numer Methods Engrg 2001;50(7):1701–36. http://dx.doi.org/10.1002/nme.93.

[21] Camanho P, Davila C. Mixed-mode decohesion finite elements in for the simulation composite of delamination materials. Nasa 2002;TM-2002-21(June):1–37. http://dx.doi.org/10.1177/002199803034505.

[22] Turon A, Camanho PP, Costa J, Dávila CG. A damage model for the simulation of delamination in advanced composites under variable-mode loading. Mech Mater 2006;38(11):1072–89. http://dx.doi.org/10.1016/j.mechmat.2005.10.003.

[23] Jensen S, Martos M, Bak B, Lindgaard E. Formulation of a mixed-mode multilinear cohesive zone law in an interface finite element for modelling delamination with R-curve effects. Compos Struct 2019;216:477–86. http://dx.doi.org/10.1016/j.compstruct.2019.02.029.

[24] Jensen S, Martos M, Lindgaard E, Bak B. Inverse parameter identification of n-segmented multilinear cohesive laws using parametric finite element modeling. Compos Struct 2019;225:111074. http://dx.doi.org/10.1016/j.compstruct.2019.111074.

[25] Turon A, Dávila CG, Camanho PP, Costa J. An engineering solution for mesh size effects in the simulation of delamination using cohesive zone models. Eng Fract Mech 2007;74(10):1665–82. http://dx.doi.org/10.1016/j.engfracmech.2006.08.025.

[26] Russo R, Chen B. Overcoming the cohesive zone limit in composites delamination: modeling with slender structural elements and higher-order adaptive integration. Internat J Numer Methods Engrg 2020;121(24):5511–45. http://dx.doi.org/10.1002/nme.6497.

[27] Davila C, Camanho P, de Moura M. Mixed-mode decohesion elements for analyses of progressive delamination. In: 19th aiaa applied aerodynamics conference. 2001, p. 1486.

[28] Falk ML, Needleman A, Rice JR. A critical evaluation of cohesive zone models of dynamic fractur. J Phys IV 2001;11(PR5):Pr5–43.

[29] Moës N, Belytschko T. Extended finite element method for cohesive crack growth. Eng Fract Mech 2002;69(7):813–33.

[30] Harper PW, Hallett SR. Cohesive zone length in numerical simulations of composite delamination. Eng Fract Mech 2008;75(16):4774–92. http://dx.doi.org/10.1016/j.engfracmech.2008.06.004.

[31] Harper PW, Sun L, Hallett SR. A study on the influence of cohesive zone interface element strength parameters on mixed mode behaviour. Composites A 2012;43(4):722–34. http://dx.doi.org/10.1016/j.compositesa.2011.12.016.

[32] Lindgaard E, Bak B, Glud J, Sjølund J, Christensen E. A user programmed cohesive zone finite element for ANSYS mechanical. Eng Fract Mech 2017;180:229–39.

[33] Remacle J, Lambrechts J, Seny B. Blossom-Quad: A non-uniform quadrilateral mesh generator using a minimum-cost perfect-matching algorithm. International 2012;(February):1102–19. http://dx.doi.org/10.1002/nme.

[34] Do BC, Liu W, Yang QD, Su XY. Improved cohesive stress integration schemes for cohesive zone elements. Eng Fract Mech 2013;107:14–28. http://dx.doi.org/10.1016/j.engfracmech.2013.04.009.

[35] Bak BL, Lindgaard E, Lund E. Analysis of the integration of cohesive elements in regard to utilization of coarse mesh in laminated composite materials. Internat J Numer Methods Engrg 2014;99(8):566–86.

[36] Guiamatsia I, Ankersen JK, Davies GA, Iannucci L. Decohesion finite element with enriched basis functions for delamination. Compos Sci Technol 2009;69(15–16):2616–24. http://dx.doi.org/10.1016/j.compscitech.2009.08.002.

[37] Guiamatsia I, Davies GA, Ankersen JK, Iannucci L. A framework for cohesive element enrichment. Compos Struct 2010;92(2):454–9. http://dx.doi.org/10.1016/j.compstruct.2009.08.028.

[38] Främby J, Fagerström M, Brouzoulis J. Adaptive modelling of delamination initiation and propagation using an equivalent single-layer shell approach. Internat J Numer Methods Engrg 2017;112(8):882–908. http://dx.doi.org/10.1002/nme.5536.

[39] Guiamatsia I, Ankersen JK, Iannucci L. A study of mixed-mode composite delamination using enriched interface elements. Aeronaut J 2013;117(1195):959–67. http://dx.doi.org/10.1017/S0001924000008617.

[40] Moslemi H, Khoei AR. 3D adaptive finite element modeling of non-planar curved crack growth using the weighted superconvergent patch recovery method. Eng Fract Mech 2009;76(11):1703–28. http://dx.doi.org/10.1016/j.engfracmech.2009.03.013.

[41] Khoei AR, Eghbalian M, Moslemi H, Azadi H. Crack growth modeling via 3D automatic adaptive mesh refinement based on modified-SPR technique. Appl Math Model 2013;37(1–2):357–83. http://dx.doi.org/10.1016/j.apm.2012.02.040.

[42] Kim J, Simone A, Duarte CA. Mesh refinement strategies without mapping of nonlinear solutions for the generalized and standard FEM analysis of 3-D cohesive fractures. Internat J Numer Methods Engrg 2017;109(2):235–58. http://dx.doi.org/10.1002/nme.5286.

[43] Guiamatsia I, Falzon BG, Davies GA, Robinson P. Improving composite damage modelling through automatic placement of cohesive elements. Collect Tech Pap - AIAA/ASME/ASCE/AHS/ASC Struct Struct Dyn Mater Conf 2008;(April):7–10. http://dx.doi.org/10.2514/6.2008-1824.

[44] Shor O, Vaziri R. Adaptive insertion of cohesive elements for simulation of delamination in laminated composite materials. Eng Fract Mech 2015;146:121–38. http://dx.doi.org/10.1016/j.engfracmech.2015.07.044.

[45] Hansbo A, Hansbo P. A finite element method for the simulation of strong and weak discontinuities in solid mechanics. Comput Methods Appl Mech Engrg 2004;193(33–35):3523–40.

[46] van der Meer FP, Sluys LJ. A phantom node formulation with mixed mode cohesive law for splitting in laminates. Int J Fract 2009;158(2):107–24. http://dx.doi.org/10.1007/s10704-009-9344-5.

[47] Areias PM, Belytschko T. Non-linear analysis of shells with arbitrary evolving cracks using XFEM. Internat J Numer Methods Engrg 2005;62(3):384–415.

[48] Chen BY, Pinho ST, De Carvalho NV, Baiz PM, Tay TE. A floating node method for the modelling of discontinuities in composites. Eng Fract Mech 2014;127:104–34. http://dx.doi.org/10.1016/j.engfracmech.2014.05.018.

[49] McElroy M. Use of an enriched shell finite element to simulate delamination-migration in a composite laminate. Compos Struct 2017;167:88–95. http://dx.doi.org/10.1016/j.compstruct.2017.01.057.

[50] Lu X, Chen BY, Tan VB, Tay TE. A separable cohesive element for modelling coupled failure in laminated composite materials. Composites A 2018;107(October 2017):387–98. http://dx.doi.org/10.1016/j.compositesa.2018.01.014.

[51] Lu X, Ridha M, Tan VB, Tay TE. Adaptive discrete-smeared crack (A-DiSC) model for multi-scale progressive damage in composites. Composites A 2019;125(January). http://dx.doi.org/10.1016/j.compositesa.2019.105513.

[52] Lu X, Chen BY, Tan VB, Tay TE. Adaptive floating node method for modelling cohesive fracture of composite materials. Eng Fract Mech 2018;194(March):240–61. http://dx.doi.org/10.1016/j.engfracmech.2018.03.011.

[53] Simo JC, Rifai MS. A class of mixed assumed strain methods and the method of incompatible modes. Internat J Numer Methods Engrg 1990;29(8):1595–638. http://dx.doi.org/10.1002/nme.1620290802.

[54] Klinkel S, Wagner W. A geometrical non-linear brick element based on the EAS-method. Internat J Numer Methods Engrg 1997;40(24):4529–45.

[55] Camanho PP, Davila CG, De Moura M. Numerical simulation of mixed-mode progressive delamination in composite materials. J Compos Mater 2003;37(16):1415–38.

[56] Dávila CG, Rose CA, Song K, et al. Superposition of cohesive elements to account for R-curve toughening in the fracture of composites. In: Abaqus users' conference. Newport, Rhode Island; 2008.

[57] Benzeggagh M, Kenane M. Measurement of mixed-mode delamination fracture toughness of unidirectional glass/epoxy composites with mixed-mode bending apparatus. Compos Sci Technol 1996;56(4):439–49. http://dx.doi.org/10.1016/0266-3538(96)00005-X.

[58] Turon A, Camanho PP, Costa J, Renart J. Accurate simulation of delamination growth under mixed-mode loading using cohesive elements: Definition of interlaminar strengths and elastic stiffness. Compos Struct 2010;92(8):1857–64. http://dx.doi.org/10.1016/j.compstruct.2010.01.012.

[59] ASTM D5528-13. Standard test method for mode i interlaminar fracture toughness of unidirectional fiber-reinforced polymer matrix composites, Vol. 2013. West Conshohocken, PA: ASTM International; 2000.